Self-heating and thermal runaway of biomass - Lab-scale experiments and modeling for conditions resembling power plant mills

Schwarzer, Lars; Jensen, Peter Arendt; Wedel, Stig; Glarborg, Peter; Karlström, Oskar; Holm, Jens Kai; Dam-Johansen, Kim

Published in:
Fuel

Link to article, DOI:
10.1016/j.fuel.2021.120281

Publication date:
2021

Document Version
Peer reviewed version

Self-heating and thermal runaway of biomass – Lab-scale experiments and modeling for conditions resembling power plant mills

Lars Schwarzer[a,1,*], Peter Arendt Jensen[a,*], Stig Wedel[a], Peter Glarborg[a], Oskar Karlström[b], Jens Kai Holm[c], Kim Dam-Johansen[a]

[a] *Department of Chemical and Biochemical Engineering, Technical University of Denmark Søltofts Plads 229, DK-2800 Kgs. Lyngby, Denmark*
[b] *Johan Gadolin Process Chemistry Centre, Åbo Akademi University, Turku FI-20500, Finland*
[c] *Ørsted A/S, Nesa Allé 1, DK-2820 Gentofte, Denmark*

Abstract

Loosely packed biomass dusts may self-heat and spontaneously ignite, especially when kept under elevated temperatures as in power plant mills. In this work, a mechanistic model was developed to predict self-ignition of biomass under such conditions. The model takes temperature- and gas phase species gradients into consideration. Reaction kinetic parameters were taken from a previous work, while material properties of biomass where found in the open literature. The model therefore did not require any parameter fitting. Model equations were discretized in one spatial dimension (here: for a cylinder). A series of lab scale experiments (10–40 g biomass dust) with beech, pine, sunflower husk pellets and wheat straw were used to validate the model. Predicted ignition temperatures were in good agreement (≈5 % error) with experimental data. A sensitivity analysis showed the model to be most sensitive to reaction kinetic parameters, and to a lesser degree towards parameters influencing heat transfer. Mass transfer limitations (oxygen diffusion) did not appear to have a significant effect on the predicted onset of ignition. A scaling study showed sample size to have a larger influence on ignition temperatures than bulk density of the sample or oxygen availability. This study demonstrates that models based on chemical kinetics, heat- and mass transfer phenomena (as opposed to numerical correlations based on the Frank-Kamenetskii method) can yield accurate predictions of

*Corresponding author
Email addresses: lars@teknologisk.dk (Lars Schwarzer), paj@kt.dtu.dk (Peter Arendt Jensen)
[1] Present address: Danish Technological Institute, Kongsvang Allé 29, DK-8000 Aarhus C, Denmark

self-ignition temperatures. It also underlines the importance of finding realistic reaction kinetic parameters for low temperatures.

1. Introduction

Biomass can replace fossil resources in a wide range of energy and material applications [1]. One example is the use of pellets made of wood or agricultural residues in combined heat and power plants with pulverized fuel boilers [2]. Like other organic substances, biomass may self-heat and spontaneously ignite under certain conditions [3]. This is a concern for storage facilities [4, 5], but also for milling equipment [6, 7]. Power plant mills are operated at elevated temperatures as a method to internally recycle heat and to pre-dry the fuel. Fuel dusts settled in power plant mills may be a source of fires [8, 9, 7, 10, 6, 11]. This is likely due to a combination of long residence times of such dust accumulations [8, 9, 10, 6] and the elevated temperatures of air and/or surfaces in mills [8, 7]. Predicting critical conditions, especially mill operating temperature, is therefore crucial for safe and economically viable use of biomass in pulverized fuel power plants.

Simple models to predict self-ignition have been based on the thermal ignition theories by Semenov [12] and Frank-Kamenetskii [13]. Scaling laws based on these theories relate the sample size in form of a characteristic dimension to critical ambient temperatures for self-ignition. Extrapolating self-ignition temperatures for solid fuels from lab scale to industrial application based on these scaling laws has been shown to lead to unreliable risk assessments [14, 15]. Some progress has been made with ignition and smoldering models that go beyond simple correlations of material properties and process parameters. Sizes of the systems modeled range from small lab-scale experiments [16, 17, 18, 19, 20] to pilot-scale setups [18, 21] and large stockpiles [22, 23, 24, 25] or silos [17, 26]. Several authors [16, 17, 20] stress the sensitivity of critical temperatures towards the reaction kinetic model used. However, only few researchers (e.g. [26, 19]) attempted to independently validate their kinetic model. Several stud-

ies [16, 17, 22, 23, 20] instead use kinetic parameters determined from hot storage tests. Extracting the kinetic parameters from such experiments is based on a Frank-Kamenetskii modeling approach, and the kinetic parameters are not necessarily free from transport limitations.

Besides the kinetic parameters, the reaction mechanisms themselves differ significantly. Models for self-ignition of stockpiles of biomass frequently require some degree of biological activity to initiate pure chemical oxidation [22, 23, 25]. Smoldering of peat was found to depend mainly on char oxidation kinetics [19], whereas ignition in packed bed has been modeled based on ignition of volatiles [21]. Power plant mills are operated in a temperature range (360–440 K) that is too high for biological activity, but too low for ignition of volatiles. Ignition is in that case likely caused by a heterogeneous oxidation of the solid biomass. This pathway is favored at lower temperatures, compared to sequential devolatilization–homogeneous ignition pathways [27, 28].

The main objective of this work is to develop and validate a simple physical model for biomass self-ignition under mill conditions, that does not require parameter fitting. Model parameters, including reaction mechanisms, are based on data available in the literature. We have recently presented a reaction mechanism for low-temperature oxidation and pyrolysis of biomass from thermogravimetric analysis [29] that will be used in the present work. Self-ignition is difficult to study in actual mills, where dust beds may accumulate over time and in different locations. Data from lab scale experiments resembling mill conditions are therefore used to validate the model. A second objective is to assess how sensitive the model is to reaction kinetic parameters and material properties.

2. Modeling

The purpose of the model is to describe self-heating and self-ignition in loosely packed beds of biomass dusts (e.g., from wood, wood pellets or agricultural residues). The model is built on the assumption that self-ignition occurs when heat released from reactions exceeds heat dissipation, resulting in thermal

runaway [12, 13]. Ignition likely occurs from a local hotspot in the dust bed [13]. At or near thermal runaway, reaction rates may also become limited by oxygen availability. To capture these effects, heat and mass transfer equations are solved in addition to reaction rates. Dust beds may have any shape, but for the sake of simplicity can be treated as ideal slabs, cylinders or spheres. Gradients are therefore resolved in one dimension only, and transport over additional sides of the bodies are set to zero. Fig. 1 shows the general concept of the model.

The model is based on the following assumptions:

- Loosely packed dust beds are porous bodies, that can be described by a split into a solid and an interstitial gas phase.
- At every point in the bed, solid and interstitial gas are in thermal equilibrium.
- Solids are isotropic and homogeneous.
- Material properties of solids are constant.
- Material properties of gases are temperature-dependent.
- Gases behave as ideal gas.
- Biomass and its components are modeled as $C_xH_yO_z$ pseudo-species, plus moisture and inert content.
- Heterogeneous oxidation and pyrolysis of the biomass, as well as evaporation of moisture occur in parallel.
- Homogeneous reactions in the gas phase are neglected.
- Reaction heats for oxidation reactions are constant; pyrolysis reactions are thermally neutral.
- Exchange of mass (gas species) with the surroundings occurs only via the bulk gas phase.
- Influence of gravity is neglected.

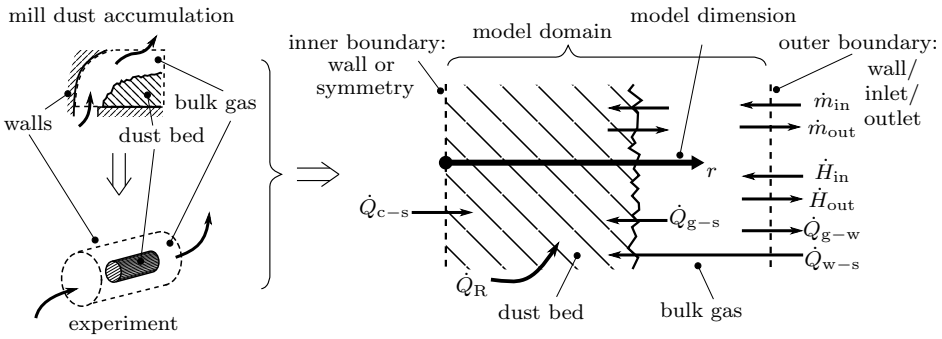

Figure 1: Geometries of actual dust beds settling in mills were simplified in the experiments (left, see following section for description). Both experiment and mill dust beds are represented by the same one-dimensional model (right), consisting of dust bed and surrounding bulk gas phase. Arrow represent flows (heat, mass) over the domain boundary (dashed outlines). $\dot{Q}_{\mathrm{R}}$ is a reaction source term. See eqs. 22–25 and text for further discussion.

2.1. Governing equations

Dust beds are considered porous solids. Within the dust bed, the split between solid and gas phase is described by the porosity ϕ,

$$\phi = 1 - \frac{\rho_{\mathrm{tot}}}{\rho_{\mathrm{s}}} = \frac{V_{\mathrm{g}}}{V_{\mathrm{tot}}} \tag{1}$$

where ρ_{tot} is the bulk density and ρ_{s} the particle density.

2.1.1. Balance equations

The dust bed zone is described by equations for the mass balance of the solid species (eq. 2), the species balance in the interstitial gas phase (eq. 3), and the heat balance in the dust bed (eq. 4):

$$\frac{\partial \rho_{\mathrm{s,i}}}{\partial t} = \dot{m}'''_{\mathrm{R,s,i}} \tag{2}$$

$$\frac{\partial C_{\mathrm{g,i}}}{\partial t} = \frac{1}{r^{\omega}} \frac{\partial}{\partial r} \left(r^{\omega}\, D\, \frac{\partial C_{\mathrm{g,i}}}{\partial r} \right) - \frac{1}{r^{\omega}} \frac{\partial}{\partial r} \left(r^{\omega}\, u\, C_{\mathrm{g,i}} \right) + \frac{\dot{n}'''_{\mathrm{R,g,i}}}{\phi} \tag{3}$$

$$\frac{\partial T}{\partial t} = \frac{1}{\rho_{\mathrm{s}}\, c_{\mathrm{p,s}} + \rho_{\mathrm{g}}\, c_{\mathrm{p,g}}} \left(\frac{1}{r^{\omega}} \frac{\partial}{\partial r} \left(r^{\omega}\, \lambda \frac{\partial T}{\partial r} \right) + \dot{Q}'''_{\mathrm{R}} \right) \tag{4}$$

In the above, r is the spatial coordinate. Gradient terms with $\partial/\partial r$ depend on the geometry, where $\omega = 0$ for slabs, $\omega = 1$ for cylinders and $\omega = 2$ for spheres.

The triple dash$'''$ on the source terms indicates a volumetric quantity. D is the diffusion coefficient, u the velocity of advective gas transport in the porous material, and λ the effective thermal conductivity of the dust bed. Fick's law of diffusion and Fourier's law of heat conduction are applied.

The bulk gas phase is described by species (eq. 5) and heat balance (eq. 6):

$$\frac{\partial C_{\mathrm{g,i}}}{\partial t} = \frac{1}{r^{\omega}} \frac{\partial}{\partial r} \left(r^{\omega}\, D \frac{\partial C_{\mathrm{g,i}}}{\partial r} \right) - \frac{1}{r^{\omega}} \frac{\partial}{\partial r} \left(r^{\omega}\, u\, C_{\mathrm{g,i}} \right) + \frac{1}{V_{\mathrm{g}}} \left(\dot{n}_{\mathrm{g,i,in}} - \dot{n}_{\mathrm{g,i,out}} \right) \tag{5}$$

$$\frac{\partial T}{\partial t} = \frac{1}{\rho_{\mathrm{g}}\, V_{\mathrm{g}}\, c_{\mathrm{p,g}}} \left(\dot{H}_{\mathrm{g,in}} - \dot{H}_{\mathrm{g,out}} + \dot{H}_{\mathrm{g,R}} + \dot{Q}_{\alpha} \right) \tag{6}$$

The $\partial/\partial r$-terms describe transport along the model dimension (diffusion, advection) and are used here to model flow to and from the dust bed. Molar streams $\dot{n}_{\mathrm{g,i,in}}$ and $\dot{n}_{\mathrm{g,i,out}}$ and enthalpy streams $\dot{H}_{\mathrm{g,in}}$ and $\dot{H}_{\mathrm{g,out}}$ describe transport over the domain boundary. The term $\dot{H}_{\mathrm{g,R}}$ is the net enthalpy flow from the dust bed to the bulk gas due to gas emissions from the reacting dust bed, and $\dot{Q}_{\alpha}$ is the net effect of heat transfer by convection between wall and gas as well as between dust bed and gas.

2.1.2. Source terms

In the above equations eqs. 2–4, terms $\dot{m}'''_{\mathrm{R,s,i}}$, $\dot{n}'''_{\mathrm{R,g,i}}$ and $\dot{Q}'''_{\mathrm{R}}$ are source terms due to reactions. Heterogeneous reactions and decomposition of solids are described by modeling the conversion $X_{\mathrm{s,i}}$ of each solid species i.

$$X_{\mathrm{s,i}} = \frac{m_{\mathrm{s,i,0}} - m_{\mathrm{s,i}}(t)}{m_{\mathrm{s,i,0}}} \tag{7}$$

Reactive species are defined to be completely convertible. The conversion rate for species i is the sum of the conversion rates in each reaction r, modeled by the following equations:

$$\frac{\mathrm{d}X_{\mathrm{s,i}}}{\mathrm{d}t} = \sum_{\mathrm{r}} \frac{\mathrm{d}X_{\mathrm{s,i,r}}}{\mathrm{d}t} \tag{8}$$

$$\frac{\mathrm{d}X_{\mathrm{s,i,r}}}{\mathrm{d}t} = k_{\mathrm{r}} \cdot (1 - X_{\mathrm{s,i}})^{\nu_{\mathrm{s,i,r}}} \cdot \prod_{\mathrm{j}} \left(\frac{p_{\mathrm{g,j}}}{p_{\mathrm{ref}}} \right)^{\nu_{\mathrm{g,j,r}}} \tag{9}$$

A power law dependence on conversion and on the partial pressure of gases j involved in the reaction is assumed, with ν as reaction orders. The reaction rate constants k_r are modeled by an Arrhenius equation:

$$k_\mathrm{r} = k_{0,\mathrm{r}} \cdot \exp\left(-\frac{E_{\mathrm{a,r}}}{R \cdot T}\right) \tag{10}$$

As a shorthand notation, a source term density z_r in units $[\mathrm{mol\,m^{-3}\,s^{-1}}]$ for each reaction is introduced, so that

$$z_\mathrm{r} = -\frac{\rho_{\mathrm{s,i,0}}}{M_{\mathrm{s,i}}\,\gamma_{\mathrm{i,r}}} \cdot k_\mathrm{r} \cdot (1 - X_{\mathrm{s,i}})^{\nu_{\mathrm{s,i,r}}} \cdot \prod_\mathrm{j} \left(\frac{p_{\mathrm{g,j}}}{p_\mathrm{ref}}\right)^{\nu_{\mathrm{g,j,r}}} \tag{11}$$

In the above equation, $\gamma_{\mathrm{i,r}} := -1$ is the stoichiometric coefficient of solid species i, i.e. reactions are scaled to consumption of one mole of i per unit volume, and $z_\mathrm{r} > 0$. The source terms can then be described by summing over all reactions (with species $j \neq i$):

$$\dot{m}'''_{\mathrm{R,s,i}} = \sum_\mathrm{r} \gamma_{\mathrm{s,i,r}} \cdot M_{\mathrm{s,i}} \cdot z_\mathrm{r} \tag{12}$$

$$\dot{m}'''_{\mathrm{R,g,j}} = \sum_\mathrm{r} \gamma_{\mathrm{g,j,r}} \cdot z_\mathrm{r} \tag{13}$$

$$\dot{Q}'''_\mathrm{R} = \sum_\mathrm{r} \Delta\overline{H}_{\mathrm{R,r}} \cdot z_\mathrm{r} \tag{14}$$

In the above, $\Delta\overline{H}_{\mathrm{R,r}}$ is the heat of reaction in $[\mathrm{J\,mol^{-1}}]$. The stoichiometric coefficients $\gamma_{\mathrm{i,r}}$ and $\gamma_{\mathrm{j,r}}$ are positive if the species is produced, negative if it is consumed and zero otherwise.

2.1.3. Transport terms

The molecular diffusion coefficient D in eqs. 3 and 5 is influenced by temperature. It can be approximated by:

$$D = D_\mathrm{ref} \left(\frac{T}{T_\mathrm{ref}}\right)^{1.75} \tag{15}$$

where diffusion coefficients D_ref at reference conditions can be found in tabulated form in the literature. The temperature exponent is theoretically limited to the interval of 1.5–2.0 [30].

Heat release and production of gaseous species drive an advective flow u, which can be modeled by Darcy's law (compare e.g. [31, 32, 19, 33, 20]):

$$u = -\frac{\kappa}{\eta} \cdot \frac{\mathrm{d}p}{\mathrm{d}r} \tag{16}$$

where κ is the permeability of the solid in units of [m^2] and η the dynamic viscosity of the gas in [Pa s].

The effective thermal conductivity appearing in eq. 4 is calculated as the sum of heat conduction in the bed and a term for radiation across pores (λ_ε) [34]:

$$\lambda = \lambda_{\mathrm{eff}} + \lambda_\varepsilon \;; \qquad \lambda_\varepsilon = K_\varepsilon \sigma\, T^3 \tag{17}$$

where σ is the Stefan-Boltzmann constant, and the proportionality factor K_ε depends on pore size and geometry. The combined equivalent thermal conductivity λ_{eff} of gas and solid is calculated from an empirical calculation, superimposing parallel and serial heat conduction [35].

$$\lambda_{\mathrm{eff}} = \lambda_{\mathrm{g}} \cdot \left(\frac{0.2}{K_{\mathrm{I}}} + \frac{0.8}{K_{\mathrm{II}}} \right)^{-1} \tag{18}$$

where K_{I} and K_{II} are the coefficients for serial conduction and parallel conduction, respectively:

$$K_{\mathrm{I}} = \left(\phi + \frac{1-\phi}{\lambda_{\mathrm{s}}/\lambda_{\mathrm{g}}} \right)^{-1} \qquad \text{and} \qquad K_{\mathrm{II}} = \phi + (1-\phi) \cdot \frac{\lambda_{\mathrm{s}}}{\lambda_{\mathrm{g}}} \tag{19}$$

2.1.4. Boundary conditions

Spatial gradients in equations 2–6 are not continuously defined at the boundaries of the model domain (compare Fig. 1) or at the interface between dust bed and bulk gas. Boundary conditions replace the missing values for heat and mass transfer.

Inflow and outflow. Gas is transported into and out of the domain via the bulk gas. The inflow of species i is given by:

$$\dot{n}_{\mathrm{i,in}} = y_{\mathrm{i,in}}\, \dot{V}_{\mathrm{in}}\, \frac{p_{\mathrm{in}}}{R\, T_{\mathrm{in}}} \tag{20}$$

where the inlet values of mole fraction y, volumetric flow rate $\dot{V}$, pressure p and temperature T are specified. The total flow rate $\dot{n}_{\mathrm{out}}$ out of the (fixed) bulk gas volume V is calculated from a constant pressure boundary condition ($p = p_0 = \mathrm{const.}$).

$$\dot{n}_{\mathrm{out}} = \dot{n}_{\mathrm{in}} + \dot{n}_{\mathrm{s-g}} - \frac{V}{R\,\Delta t} \cdot \left(\frac{p_0}{T} - \sum_{\mathrm{j}} C_{\mathrm{j}} \cdot R \right) \tag{21}$$

The molar flow rates of each species at the outlet $\dot{n}_{\mathrm{i,out}}$ are calculated from the mole fractions in the bulk gas $y_{\mathrm{i,g}}$ and the total flow rate.

Enthalpy transported in and out of the domain can be calculated from the total molar flow rates, specific heat capacity, and inlet temperature ($\dot{H}_{\mathrm{in}}$) or bulk gas temperature ($\dot{H}_{\mathrm{out}}$). At the interface between dust bed and bulk gas phase, similar terms appear in eqs. 3 and 5 to describe diffusion and advection. Gradients $\partial/\partial r$ can therefore be evaluated continuously on both sides of the interface.

External heat transfer. External heat transfer, here expressed as heat flux $\dot{Q}''$, appears as radiation between wall and solid (eq. 22), convection between gas and solid (eq. 23), convection between gas and wall (eq. 24), and for slab geometries also as conduction at the solid contact (eq. 25):

$$\dot{Q}''_{\varepsilon,\mathrm{w-s}} = \varepsilon \cdot \sigma \cdot (T_{\mathrm{w}}^4 - T_{\mathrm{s}}^4) \tag{22}$$

$$\dot{Q}''_{\alpha,\mathrm{g-s}} = \alpha_{\mathrm{g-s}} \cdot (T_{\mathrm{g}} - T_{\mathrm{s}}) \tag{23}$$

$$\dot{Q}''_{\alpha,\mathrm{g-w}} = \alpha_{\mathrm{g-w}} \cdot (T_{\mathrm{g}} - T_{\mathrm{w}}) \tag{24}$$

$$\dot{Q}''_{\lambda,\mathrm{c-s}} = \frac{\lambda_{\mathrm{c}}}{s_{\mathrm{c}}} \cdot (T_{\mathrm{c}} - T_{\mathrm{s}}) \tag{25}$$

In the above equations, ε is the effective emissivity, σ is the Stefan-Boltzmann constant, α are heat transfer coefficients, λ_{c} the thermal conductivity of the contacting structure and s_{c} its wall thickness. The above (eqs. 22–23) are boundary conditions for eq. 4 that replace $\lambda\,\partial T/\partial r$ at the dust bed/bulk gas interface. Eqs. 23 and 24 are the boundary conditions for the bulk gas phase, where

$\dot{Q}_\alpha = \int \dot{Q}''_\alpha \mathrm{d}A$ in eq. 6. Eq. 25 only appears for slab geometries. The effective emissivity ε depends on the geometry, as well as on the emissivities of sample (ε_s) and wall (ε_w). Heat transfer coefficients α can be found from Nusselt-number correlations.

2.2. Model implementation and discretization

The model calculations were carried out for cylinder geometries, representing the samples used in the experimental part of this work (see description in the following section). The dust bed was discretized into cells of finite volume along the cylinder radius (the model dimension in Fig. 1). Grid refinement was checked by simulations on grids with 5, 10, 20, 50 and 100 cells. The 50-cell grid was seen as sufficiently accurate and used in all further simulations. The bulk gas phase was represented by a single cell. Equations 2–6 were integrated over the finite volume cells. Changes in one volume due to diffusive and advective transport can be expressed by the flux across the boundary to and from neighboring volumes. Boundary conditions (as described above) replace the flux terms at the inner and outer boundaries (compare Fig. 1). An implicit scheme (backward Euler) is applied to the diffusive terms (heat conduction, gas diffusion) in equations 3, 4 and 5. Implicit schemes are unconditionally stable (see e.g. [36]). A first order upwind scheme is used to determine the concentrations in the advective terms ($C_{\mathrm{g,i}}\, u$) in equations 3 and 5. Solutions for the equation system in each timestep are found by an inner iteration loop. The calculation moves on to the next timestep if the inner iteration converges. The width of the timestep is adapted to the heat release and oxygen consumption rates at runtime. This allows the solver to march forward faster when reaction rates are low, while providing better temporal resolution in the ignition phase. More details can be found in the supporting information.

2.3. Model parameters

Mass conversion, heat release, as well as production and consumption of chemical species are followed. Gaseous species released during smoldering or

pyrolysis of biomass are CO, CO_2, water vapor, H_2, hydrocarbons and organic volatiles (e.g., furans and phenolic compounds) [37, 38, 39, 40, 41, 42, 43]. With respect to self-heating and ignition, tracking consumption of oxygen is the main purpose of the species model. The types of reactions considered in the model are heterogeneous oxidation (R1), pyrolysis (R2), and evaporation of water (R3):

$$\text{organic solid} + O_2 \rightarrow CO_2 + CO + H_2O_{(g)} \tag{R1}$$

$$\text{organic solid} \rightarrow CO_2 + CO + H_2O_{(g)} + \text{tars and volatiles} \tag{R2}$$

$$\text{moisture} \rightarrow H_2O_{(g)} \tag{R3}$$

All other reactions, such as homogeneous gas phase reactions and condensation of water vapor, are neglected. The authors have recently presented kinetic models for biomass pyrolysis and oxidation determined in the temperature range of 423–523 K, which will be implemented here [29]. In these models, *organic solid* is an umbrella term for the volatilizable fractions of extractives, hemicelulose, lignin and cellulose, respectively, plus char. These are tracked individually as (pseudo-)species in the model, i.e. a reaction of type R1 is solved for each of the five organic species and one reaction of type R2 for each of the four volatilizables. Char can only undergo oxidation. It had previously been investigated whether the oxidation reactions for extractives, hemicellulose, lignin and cellulose could be represented by the same kinetic parameters (*Model I*) or whether they instead are best represented by individiual kinetic parameters (*Model II*). Both kinetic models were also used in this study. A full description of the kinetic models, including numerical values of the rate constants and procedure for determining the split between volatilizable fractions and char, can be found elsewhere [29].

Water evaporation (R3) is treated as a single first-order Arrhenius reaction. Evaporation is treated in a simplified manner, as the self-ignition temperatures in the range of interest in this study (>423 K) are greater than those necessary to dry the samples. Rate parameters used are $k_0 = 3 \times 10^{-7}\,\mathrm{s}^{-1}$ and $E_\mathrm{a} = 65\,\mathrm{kJ\,mol}^{-1}$, and the enthalpy of evaporation is $\Delta H_\mathrm{evap} = 40.66\,\mathrm{kJ\,mol}^{-1}$. Parameters were found by averaging over literature values [19, 44].

To calculate oxygen consumption and production of CO and CO_2, a pseudo composition $C_xH_yO_z$ is assigned to the solid organic fraction of each biomass. Values for carbon, hydrogen and oxygen fractions are taken from the elemental analyses (Table 2), The organic fraction of beech is represented by $C_{30}H_{40}O_{19}$, pine by $C_{30}H_{42}O_{18}$, sunflower by $C_{30}H_{41}O_{22}$ and wheat by $C_{30}H_{42}O_{21}$. Differences between the components extractives, hemicellulose, lignin, cellulose and char are neglected in this model, although they may vary to some degree (see e.g. [45]). The split between CO and CO_2 for pyrolysis and oxidation reactions, $\gamma_{CO}/\gamma_{CO_2}$, was estimated from experimental data.

The heat of reaction for oxidation reactions is calculated from the lower heating value of the biomass, where incomplete conversion of carbon is neglected:

$$\begin{aligned}\Delta\overline{H}_{R,ox} &= h_{LHV} \cdot M_{fuel} - \Delta\overline{H}_{R,CO,ox} \cdot \frac{\gamma_{CO}}{\gamma_{CO} + \gamma_{CO_2} + \gamma_{H_2O}} \cdot \frac{\gamma_{CO}}{\gamma_{fuel}} \\ &\approx h_{LHV} \cdot M_{fuel} \end{aligned} \tag{26}$$

Oxidation of CO to CO_2 has a heat of reaction of $\Delta\overline{H}_{R,CO,ox} = 283\,\mathrm{kJ\,mol^{-1}}$ (calculated based on the enthalpy of formation of both gases [46]), while the $h_{LHV} \cdot M_{fuel}$-term is $>10\,\mathrm{MJ\,mol^{-1}}$. The error introduced by neglecting the correction term is approximately 5 %. This was judged to be less than the conceptual uncertainty, and the sensitivity to the lower heating value h_{LHV} was investigated instead of correcting for incomplete oxidation. Pyrolysis is assumed to be thermally neutral ($\Delta\overline{H}_{R,pyr} = 0$). In general, biomass pyrolysis includes both exothermic and endothermic processes [47, 48].

Material properties appear in equations for heat and mass transfer. Parameters can be grouped into those of the biomass proper (λ_s, ρ_s, $c_{p,s}$), those of the dust bed (K_ε, κ), as well as gas phase properties (λ_g, ρ_g, $c_{p,g}$, η_g), gas mixture properties (D_{ref}), and radiation parameters (ε). Gas phase properties for N_2, O_2, CO_2, CO and H_2O are well-established and available in reference works as a function of pressure and temperature. Other parameters are known less accurately or show a higher natural variation (Table 1). A set of base case parameters was established from the literature. Parameter uncertainties were

further evaluated by a sensitivity analysis.

3. Experimental

3.1. Setup

A lab scale setup was used to investigate under which conditions self-ignition occurs in loosely packed dust beds. The arbitrary shapes and sizes of settled dust beds were simplified. A cylindrical shape of sample holder and surroundings was chosen for the experiments. Samples were filled lightly (without compaction) into a wire mesh basket (length 150 mm, diameter 30 mm), that was suspended centrally in a tubular oven (length 955 mm, inner diameter 51 mm), Fig 2. Using a wire mesh basket ensured that samples had a geometrically defined shape, while still permitting gas exchange with the surrounding oven. The symmetry of the cylindrical basket could be exploited in modeling. Heat was supplied externally by three independent thermocontrollers. Temperatures were measured by type-K thermocouples in the sample center, at the outer sample surface, in the gas phase around the sample and at the oven wall.

Pre-set mixtures of oxygen and nitrogen were supplied to the oven at one end, with total flow rates set between 1–2.5 L min^{-1}. Extracting all gas at the opposite end created a constant flow through the reactor. The gas was filtered, dried, and analyzed for CO (ranges 0–4000 ppm and 0–30 %), CO_2 (0–3000 ppm and 0–20 %) and O_2 (0–25 %). When comparing emissions from samples of different original mass, measured gas concentrations were converted to molar

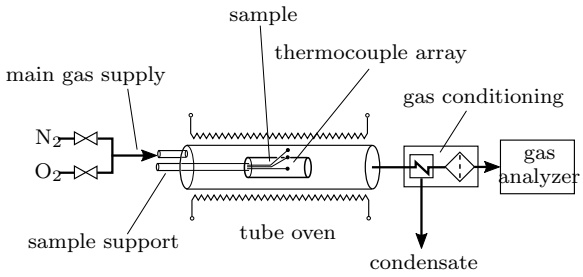

Figure 2: Experimental setup, simplified

Table 1: Parameters used in base case simulations. Parameter ranges were taken from the literature, unless otherwise noted. The parameter set for the base case was chosen based on most commonly occuring values.

parameter	units	base value	range	source/estimated from
λ_s	$W\,m^{-1}K^{-1}$	0.2	0.1–0.6	[49, 35, 50, 51]
ρ_s	$kg\,m^{-3}$	600	200–1000	[52, 49, 35, 51]
$c_{p,s}$	$J\,kg^{-1}K^{-1}$	2000	1100–2100	[53, 54, 50, 55]
K_ε	m	10^{-3}	10^{-5}–10^{-2}	[31, 19]
κ	m^2	10^{-10}	10^{-12}–10^{-7}	[31, 24]
D_{ref}	$10^{-5}\,m^2\,s^{-1}$	1.5	1.3–2.2	[30, 56]
ε_s	–	0.8	0.4–0.9	[57, 35]
ε_w	–	0.8	0.6–0.9	[35]
$\gamma_{CO}/\gamma_{CO_2}$	–	0.5	0.2–0.8	estimate from experiments

release rates (based on the total gas flow rate) and scaled by initial sample mass, i.e., expressed in $mol\,s^{-1}kg^{-1}$. During the experiments, significant amounts of tar precipitated throughout the gas conditioning unit. Since these could not be collected in a defined way, they were not analyzed.

Temperature and gas measurements experienced different signal delay times. While thermocouples were taken to respond immediately to temperature changes, the gas analyzers reacted with approximately two minutes delay to oxygen pulses. Data were synchronized by shifting the gas analysis data forward in time. Appropriate delay times were determined for each experiment individually, bases on oxygen pulses. Further details can be found in [58].

3.2. Materials

To cover the range of fuel used in thermal power plants [1, 2], four biomasses were used in this study: beech wood, pine wood, commercial sunflower husk pellets and wheat straw. For these biomasses, reaction kinetic models have been determined in a previous work of the authors [29]. All materials were used

in pulverized form. Beech and pine were selected as typical representatives of hard- and softwood. Wood samples were bark-free. Sunflower husks and wheat straw represent two typical agricultural residues used as fuels, where sunflower husks are comparatively rich in extractives. Extractives are thought to promote self-ignition [59, 60]. Relevant composition data are summarized in Table 2. Heating values were determined according to EN 14918, proximate analysis was carried out according to ISO 18134-1, ISO 18122 and ISO 18123, and major elements C, H, N were determined according to ISO 16948 by an external lab. Klason lignin and carbohydrate composition of the six samples were determined by sulfuric acid hydrolysis, details can be found elsewhere [29].

In this study, all samples were used as-is, i.e., without prior drying or other treatment. Bulk density was determined by weighing the samples on a Mettler Toledo scale and dividing the mass by the (nominal) volume of the samle holder.

3.3. Procedure

A typical experiment consisted of inserting the sample into the cold oven, setting and controlling the gas flow rates, and only then starting the heating program. Heating programs used here consisted of a 'ramp' and a 'holding' phase. During the ramp phase, setpoint temperatures were increased linearly. During the holding period, the oven temperature was kept constant. Experiments at constant heating rate have previously been proposed by other authors [61, 62] – as opposed to exposing fresh samples to incrementally higher constant temperatures on separate experiments. A possible drawback is that the external heating may be faster than self-heating, making the latter difficult to identify. By estimate calculations, it was concluded that self-heating would become apparent from temperatures of 380–500 K upwards under the conditions used here (see supporting information).

A series of scanning experiments were carried out by heating at a constant rate beyond estimated critical temperatures (typically to 573 K). Ignition was defined by a 60 K overshoot of the sample center temperature compared to the oven temperature. The oven temperature when this occurred is referred to as

Table 2: Proximate, elemental and compositional analysis of the biomasses used used in this study. Difference to one in the sum of the compositional analysis is balance error.

	Beech wood	Pine wood	Sunflower	Wheat straw
Particle size [µm]	0–200	50–200 600–1000	125–850	200–400
Bulk density [kg/m^3]	160	76–198	377	104
Heating value (daf) [MJ/kg]	19.15	19.80	20.46	18.20
Proximate analysis, dry base [kg/kg]				
Volatiles	0.771	0.856	0.756	0.774
Char	0.202	0.141	0.193	0.184
Ash	0.027	0.003	0.052	0.042
Moisture (average, from TGA)	0.059	0.049	0.085	0.061
Elemental analysis, dry base [kg/kg]				
C	0.512	0.528	0.521	0.480
H	0.057	0.061	0.059	0.057
O (by difference)	0.429	0.410	0.503	0.457
N	0.002	0.001	0.015	0.004
Compositional analysis, dry base [kg/kg]				
Glucose (total)	0.337	0.440	0.270	0.424
Non-glucose carbohydrates	0.225	0.228	0.273	0.333
Klason lignin	0.346	0.278	0.316	0.208
Extractives	0.015	0.093	0.089	0.039
Sum (composition)	0.923	1.039	0.948	1.004
Lignin ash	0.009	0.002	0.006	0.014

ignition temperature T_{ign} in the following, the corresponding time to ignition is given by t_{ign}.

To determine critical ambient temperatures for ignition, further experiments were carried out at different final oven temperatures. Final oven temperatures were varied in 5 K intervals under a set of otherwise equal conditions. A test result was treated as ignition (supercritical), if the temperature in the sample increased by more than 60 K compared to the surrounding oven temperature. Conditions under which ignition did not occur are referred to as subcritical. Critical ambient temperatures T_{crit} are then defined as the mean between the highest final oven temperature under which the sample remained subcritical and the lowest final temperature under which the sample became supercritical. For the 5 K interval used, critical temperatures could be determined with ± 2.5 K accuracy.

Additional experiments were run in inert atmosphere (100 % nitrogen) to determine whether exothermal pyrolysis reactions contribute to self-heating. Heating programs were the same as for the experiments run in oxidative atmosphere.

4. Results and discussion

4.1. Experimental

Supercritical self-heating can be clearly distinguished from subcritical self-heating, and both are distinct from pyrolysis (Fig. 3). In the pyrolysis experiment, temperatures in the sample center reach, but do not exceed, oven wall temperatures (Fig. 3a). No relevant self-heating occurs in an inert atmosphere for the temperatures and sample conditions investigated. Subcritical self-heating results in a mild temperature overshoot (16 K in the case shown). Reactions then stabilize for some time, as indicated by approximately constant temperatures in the sample center (Fig. 3a) in addition to near-constant CO and CO_2 concentrations (Fig. 3b). Supercritical self-heating leads to ignition and burnout of the sample, as seen by the sudden, large increase in sample center

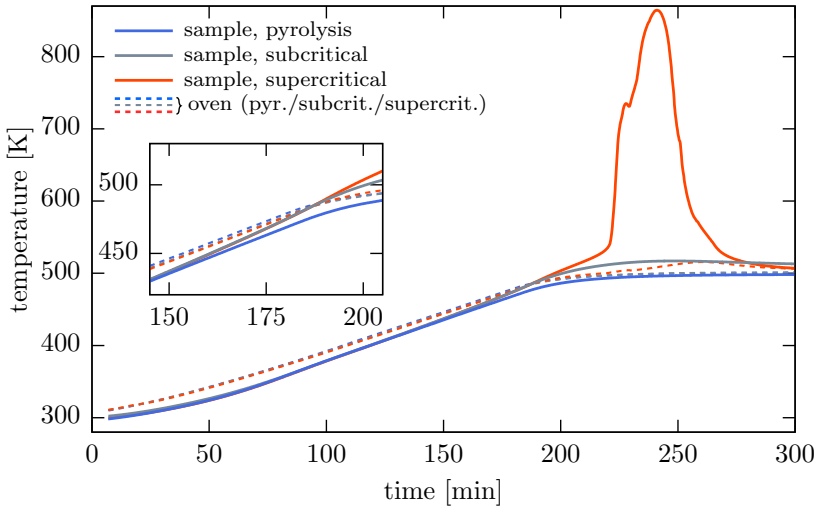

(a) Temperatures

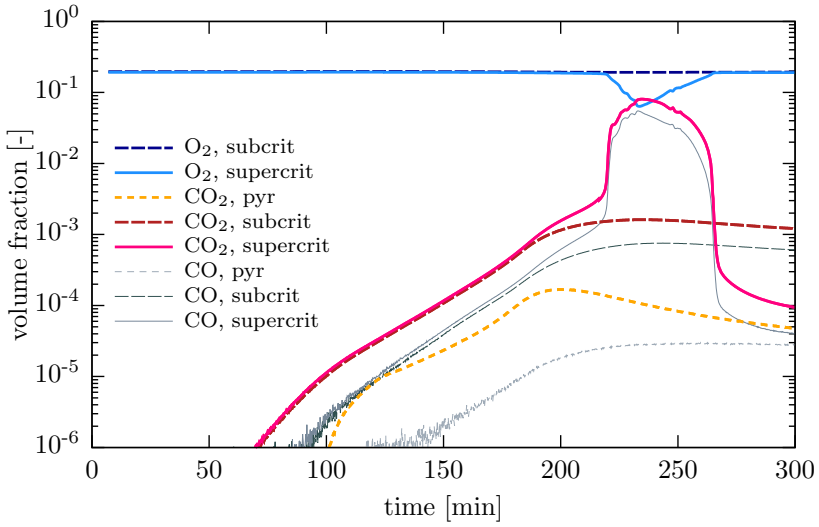

(b) Gas volume fractions, dry

Figure 3: Typical experimental results for pine, 50–200 µm particle size, heated at 1 K/ min to 498 K (pyrolysis, subcritical) and 503 K (supercritical), respectively.

temperature (Fig. 3a). Experimental oven temperatures show a slight peak for the supercritical experiment around 210–290 min. This is likely caused by the heat released during burnout of the sample. Ignition is further accompanied by significant consumption of oxygen, as well as release of larger amounts of CO and CO_2 when compared to subcritical self-heating (Fig. 3b). By comparing both subcritical and supercritical experiments to pyrolysis experiments, it is apparent that CO and CO_2 to a large degree come from oxidation reactions (note the logscale in Fig. 3b). Furthermore, smoldering oxidation reactions are measurable by CO and CO_2 emissions (1 ppm each around 70 minutes and 90 minutes, respectively, in the experiments in Fig. 3) before self-heating becomes measurable (by a divergence between sample center temperatures for oxidation and pyrolysis experiments around 150 minutes). The temperature at which self-heating is detectable, ≈440 K, falls within the range of values expected (see supporting information).

4.2. Modeling thermal runaway and T_{ign}

All samples ignited in the series of scanning experiments run by heating at 1 K/ min to 573 K in 20 % oxygen. Qualitatively, model predictions are in good agreement with measured data, showing an initial heating phase followed by thermal runaway (Fig. 4). Corresponding oxygen concentrations in the bulk gas phase/oven outlet can be found in the supporting information. Boundary and initial conditions for the simulations (time-dependent oven temperatures, inlet oxygen concentration, sample mass) were taken from the respective experiments. At thermal runaway, several modeling assumptions no longer hold, and calculations were stopped.

Quantitatively, the ignition temperatures predicted in the simulations ($T_{\mathrm{ign,sim}}$) are always lower than those measured, Fig. 4 and Table 3. Relative errors δ_{T} were quantified by:

$$\delta_{\mathrm{T}} = \frac{T_{\mathrm{ign,sim}} - T_{\mathrm{ign,exp}}}{T_{\mathrm{ign,exp}}} \tag{27}$$

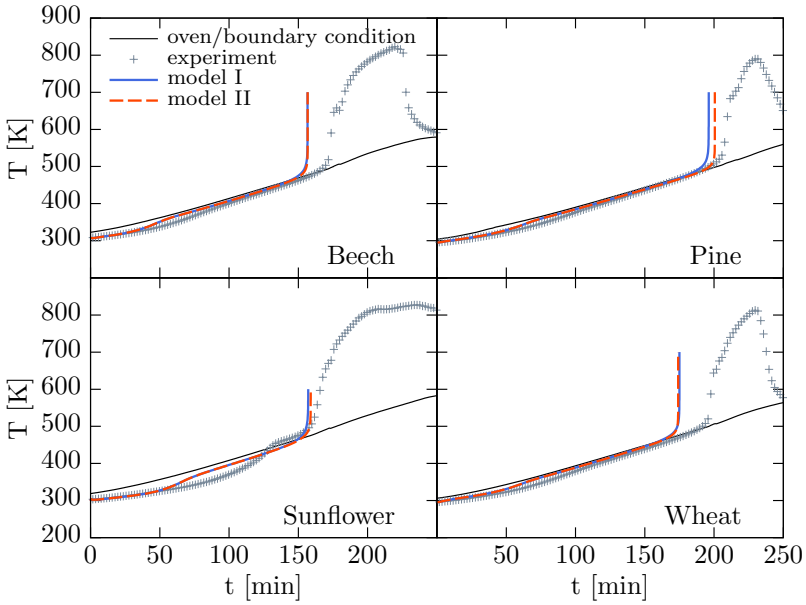

Figure 4: Comparison of measured and modeled time-temperature histories for different biomasses. Samples heated at 1 K/ min to 573 K in 20 % oxygen atmosphere (nominal values). Measured oven wall temperatures were used as boundary conditions in the simulations.

Table 3: Ignition temperature model validation: relative errors δ_T are within −1 % to −5.5 %. Simulation boundary and initial conditions were taken from experimental data.

	experiment			model I		model II	
sample	$y_{O_2,in}$ [%]	m_0 [g]	T_{ign} [K]	T_{ign} [K]	δ_T [%]	T_{ign} [K]	δ_T [%]
beech	19.4	17.0	496.1	476.6	−3.9	476.8	−3.9
pine	19.7	12.9	507.4	493.1	−2.8	498.4	−1.8
sunflower	19.3	40.0	480.6	473.4	−1.5	475.8	−1.0
wheat	19.4	11.0	501.8	475.9	−5.2	475.1	−5.3

Model errors differed slightly among the biomasses tested. With all other parameters equal, kinetic models I and II (see section 2.3) resulted in very similar predictions. This is in agreement with the kinetic study [29], were results between models I and II also did not differ significantly below 523 K. In the beginning of the experiment (0–100 min), temperatures in the sample are likely governed by external heating and the evaporation of fuel moisture. Simulated sample temperatures follow the oven temperature more closely than those measured. This behavior suggests that heat transfer to and through the sample is overpredicted, and that evaporation in the model is faster than observed experimentally. At thermal runaway, self-heating rates were measured up to 60 K min^{-1}. Simulated rates could reach several hundred Kelvin per second, i.e. orders of magnitude larger (compare Fig 5a). Similar overly steep temperature gradients have also been reported by other researchers [63, 24]. Probable causes for the discrepancies in this work are that the kinetic mechanism is valid for low heating rates ($\leq$5 K min^{-1}) and temperatures ($\leq$550 K) [29], that diffusion is calculated relative to a fixed reference frame instead of as counterflow diffusion [64], and that influences of structural changes in the biomass on thermal conductivity [65] and specific heat capacity [55] are neglected. All of these may affect the rate of temperature increase after ignition, but should have little influence on ignition onset itself.

Simulated radial profiles of temperature and oxygen around the time of thermal runaway show ignition occurs at a hotspot in the center of the sample (Fig. 5). This agrees with measured data from sample center and boundary (data not shown), where the sample center temperatures exceed those at the boundary during ignition and burnout. Slow heat dissipation from the sample center outwards promotes thermal runaway. Up to a sample center temperature of approximately 650 K (at 11 766.87 s), oxygen distribution is relatively homogeneous over the sample radius. This suggests that mass transport limitations (especially diffusion) have little influence in the early stages of thermal runaway. Model results were checked for plausibility with a simple engineering calculation (see supporting information). Estimated Damköhler numbers, i.e., the ratio be-

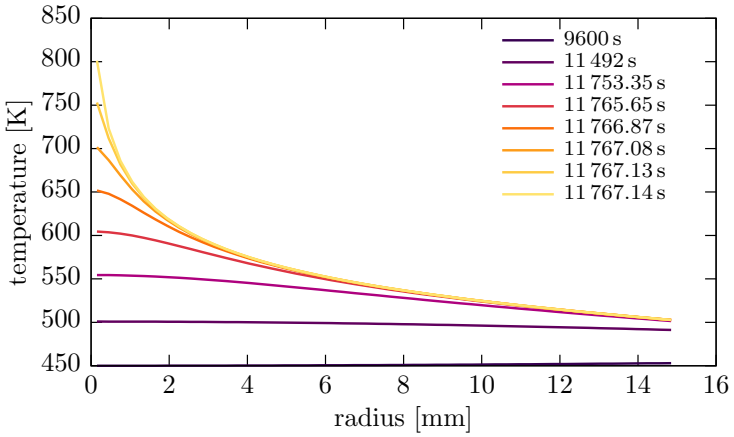

(a) Temperature

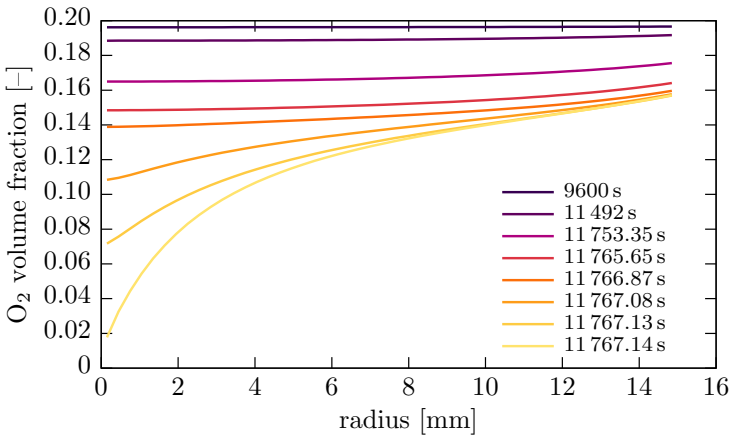

(b) Oxygen

Figure 5: Radial profiles at the onset of thermal runaway. Pine, model I, heated at 1 K/ min to 573 K. Compare Fig. 4, top right

tween reaction rate to mass transfer rate, suggested that oxygen diffusion into the sample is much faster than oxygen depletion by reactions up to 550 K for this experiment.

4.3. Modeling critical temperatures T_{crit} and mass loss

The ignition temperature T_{ign} (as modeled in the previous section 4.2) can serve as a proxy for the critical ambient temperatures T_{crit}. The value of these temperatures can differ, especially when the oven temperature continues to ramp up after thermal runaway has been initiated ($T_{\mathrm{ign}} \geq T_{\mathrm{crit}}$, compare definitions in section 3.3). The second series of experiments under subcritical and supercritical conditions were therefore simulated to compare measured and modeled critical ambient temperature.

Determining critical temperatures in the simulation is done in the same indirect way as in the experiments: simulations are repeated while varying the final wall temperature and registering whether ignition occurs or not under a given set of conditions. In this case, wall temperatures used as boundary conditions were modified by a factor τ, where $T_{\mathrm{w,sim}} = \tau \cdot T_{\mathrm{w,exp}}$ (Fig. 6). The value of $(1 - \tau)$ is a measure of simulation deviation (4 % for the example shown). Simulations using oven temperatures from a subcritical experiment were repeated while lowering values for τ in 0.01 increments. Once a value for τ was found for which the simulation predicted no ignition, results were checked by simulating a corresponding supercritical experiment with the same factor for the boundary condition. As expected, the simulations predicted that the sample ignites. However, ignition appeared slightly delayed in the simulations.

4.4. Modeling subcritical mass loss Δm

Simulations of subcritical oxidation experiments and pyrolysis experiments were used to validate the mass loss predicted by the model (Table 4). Relative errors for mass δ_{m} were defined in analogy to those for temperature:

$$\delta_{\mathrm{m}} = \frac{\Delta m_{\mathrm{sim}} - \Delta m_{\mathrm{exp}}}{\Delta m_{\mathrm{exp}}}; \qquad \Delta m = m_0 - m_{\mathrm{f}} \tag{28}$$

Table 4: Mass loss model validation for subcritical oxidation and pyrolysis: Mass loss $\Delta m = m_0 - m_\mathrm{f}$ is predicted too low in oxidation experiments and too high in pyrolysis experiments. Oven temperatures used as boundary conditions had to be lowered ($\tau < 1$) to prevent ignition in subcritical simulations. Pyrolysis kinetics are the same for both model I and II (lower part of the table). Abbreviations: c = coarse (600–1000 µm particles), f = fine (50–200 µm particles). See text for discussion.

	experiment					model I			model II		
sample	$T_{\mathrm{w,f}}$	$y_{\mathrm{O_2,in}}$	t_f	m_0	Δm	τ	Δm	δ_m	τ	Δm	δ_m
	[K]	[%]	[min]	[g]	[g]	[–]	[g]	[%]	[–]	[g]	[%]
pine (f)	500	19.5	417	8.05	1.97	0.96	1.38	−30	0.97	1.27	−36
pine (f)	502	19.6	359	10.01	2.39	0.96	1.62	−32	0.97	1.48	−38
pine (f)	501	19.7	948	10.55	4.85	0.96	3.59	−26	0.97	2.72	−44
pine (f)	502	19.6	347	12.00	2.62	0.95	1.70	−35	0.97	1.83	−30
pine (c)	501	19.6	414	14.99	4.08	0.95	2.44	−40	0.97	2.58	−37
pine (c)	496	19.6	593	18.15	4.71	0.96	4.18	−11	0.97	3.32	−29
pine (f)	517	7.9	608	10.80	5.05	0.94	2.78	−45	0.95	2.41	−52
pine (c)	512	8.1	432	18.46	5.58	0.94	3.42	−39	0.95	3.05	−45
beech	581	0	377	17.00	10.03	1	10.70	7			
pine (f)	579	0	646	10.38	7.02	1	8.06	15			
sunflower	581	0	348	40.00	22.28	1	24.62	10			
wheat	580	0	371	11.00	6.65	1	7.63	15			

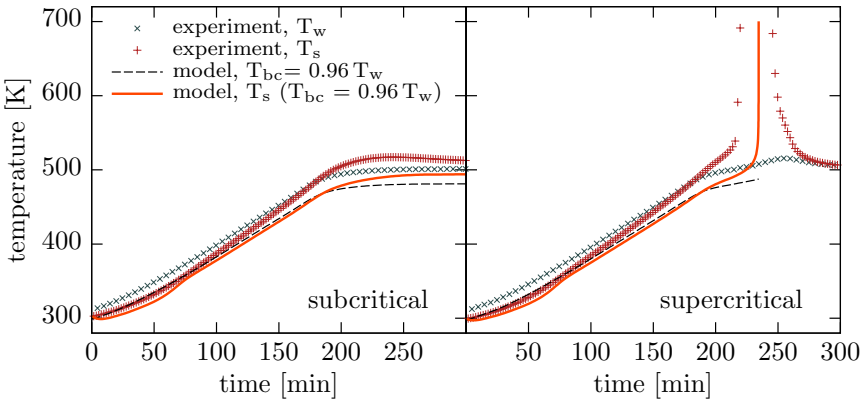

Figure 6: Critical temperatures for thermal runaway are modeled by introducing a correction τ for the wall temperature (see text for discussion). Pine, 20 % oxygen; kinetic model I, $\tau = 0.96$. Experimental data are from the experiments shown in Fig. 3a.

As discussed above, the wall boundary condition $T_{\mathrm{w,sim}}$ was lowered compared to the measured temperature $T_{\mathrm{w,exp}}$ to prevent ignition in the subcritical simulations. Values of τ were between 0.94–0.96 for model I and within 0.97–0.95 for model II. The simulations predicted lower mass loss (i.e., higher residual masses) in all oxidation cases (Table 4). This may be a result of the lower simulated temperatures also within the dust bed, compared to those measured (compare the subcritical cases in Fig. 4). For pyrolysis, mass loss is slightly overpredicted, when $\tau = 1$ (Table 4). Relative mass loss errors δ_{m} interestingly do not seem to correlate with the duration of the experiment t_{f}. Model predictions are better for $y_{\mathrm{O_2,in}} \approx 20\,\%$ than for $\approx 8\,\%$ oxygen, both when δ_{m} and when τ are considered. Given the relative simplicity of the model and the absence of fitting parameters, the overall agreement between model and experiment is good.

4.5. Sensitivity analysis

For the sensitivity analysis, two test cases were used. The test cases differed in their thermal boundary conditions: For a 'static' test case, wall temperatures were kept constant in time, and gas inlet and wall temperatures were equal. The sensitivity of the critical temperature T_{crit} to parameters was investigated

by varying the boundary condition temperatures in 0.5 K intervals, and checking whether or not ignition would occur in the simulations. The calculations were carried out for: pine, model I, dry sample, 20.0 % oxygen, bulk density 120 kg m^{-3}. For the base case, ignition was predicted for $T_{\mathrm{crit}} = 479$ K. To test the dynamic behavior, an experimental oven temperature history was used as boundary condition (pine, model I, heated at 1 K min^{-1} from ambient to 573 K in 19.7 % oxygen atmosphere, 12.9 g sample mass). The sensitivity of time to ignition t_{ign} ignition and temperature T_{ign} was evaluated. Ignition occurs at $t_{\mathrm{ign}} = 11\,753.3$ s with $T_{\mathrm{ign}} = 493.0$ K in the base case. The constant heating rate used in the dynamic simulations means that ignition time and temperature are coupled.

Material and transport properties were varied by ±10 %, ±25 % and ±50 % around the base case values, as well as within boundaries found in the literature (compare Table 1). The pre-exponential factor k_0 of the Arrhenius expression, the lower heating value h_{LHV} and the split between CO and CO_2 were also varied by ±10 %, ±25 % and ±50 % around the base case values. Effects of activation energy E_{a} are discussed separately below. The sensitivity analysis was run by varying one parameter at a time, keeping the others at the values defined for the base case calculations.

Varying parameters by the same factor (e.g., 25 %) allows to assess the (relative) numerical importance of a parameter. Several parameters have a non-linear influence, and the sensitivity towards their value is not necessarily symmetric (Fig. 7). Values for the full sensitivity analysis can be found in the supporting information. Clearly, the model is most sensitive to parameters governing reaction heat release (k_0 and h_{LHV}), and secondly to parameters influencing heat transfer and absorption (λ_{s}, ε_s, $c_{\mathrm{p,s}}$, ρ_{s}). Mass transfer parameters (κ, D_{ref}) have very little influence, in agreement with the radial profiles shown in Fig. 5.

In practice, some parameters (e.g., $c_{\mathrm{p,s}}$, λ_s) are known with a much higher accuracy than others (e.g., κ, K_ε). Varying parameters within plausible limits allows to assess the conceptual uncertainty of the model (Table 5). Relatively large effects are seen for parameters influencing the heat balance, especially ther-

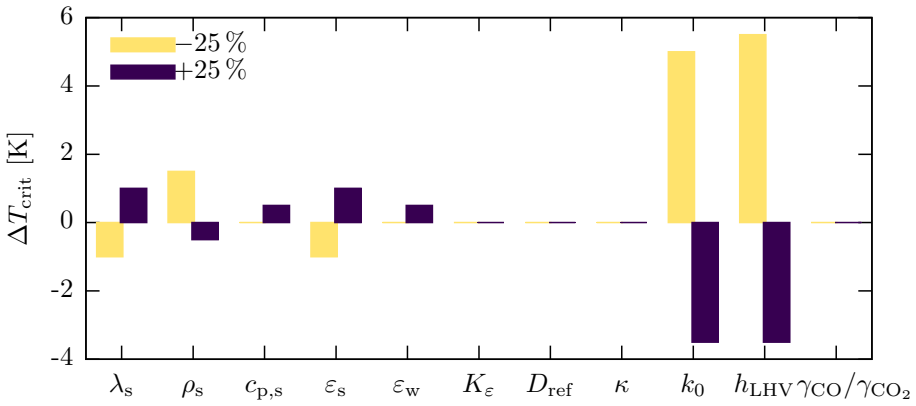

Figure 7: Sensitivity analysis: effect of varying parameters by ±25 % on the modeled critical temperature (Base case: $T_{\mathrm{crit}} = 479\,\mathrm{K}$)

Table 5: Sensitivity analysis: Effect of varying modeling parameters within a range of plausible values on critical ambient temperature T_{crit} in static simulations and on time to ignition t_{ign} in dynamic simulations. Base cases: $T_{\mathrm{crit}} = 479\,\mathrm{K}$, $t_{\mathrm{ign}} = 11\,753.3\,\mathrm{s}$

			minimum			maximum		
parameter	units	base	value	ΔT_{crit} [K]	Δt_{ign} [s]	value	ΔT_{crit} [K]	Δt_{ign} [s]
λ_{s}	$\mathrm{W\,m^{-1}K^{-1}}$	0.2	0.1	−2.5	−62.9	0.6	5	148
ρ_{s}	$\mathrm{kg\,m^{-3}}$	600	200	6	188	1000	−1.5	−41.6
$c_{\mathrm{p,s}}$	$\mathrm{J\,kg^{-1}K^{-1}}$	2000	1100	0	−247	2100	0	26.3
K_{ε}	m	10^{-3}	10^{-5}	−1	−31.4	10^{-2}	7	225
κ	$\mathrm{m^2}$	10^{-10}	10^{-12}	0	−2.2	10^{-7}	0	23.6
D_{ref}	$10^{-5}\,\mathrm{m^2\,s^{-1}}$	1.5	1.3	0	2.0	2.2	0	−4.3
ε_{s}	–	0.8	0.4	−3	−53.8	0.9	0.5	11.3
ε_{w}	–	0.8	0.6	0	−2.3	0.9	0.5	0.8
$\gamma_{\mathrm{CO}}/\gamma_{\mathrm{CO_2}}$	–	0.5	0.2	0	−1.3	0.8	0	0.9

mal conductivity λ_s, density ρ_s, and the coefficient for radiative heat transfer in a porous solid K_ε. Larger values of λ_s and K_ε increased the thermal diffusivity, inhibiting ignition. Larger solid densities (at constant bulk density) had the opposite effect (lowering the effective thermal conductivity for constant λ_s via larger porosity ϕ). Effects of varying thermal conductivity and solid density cancelled, when the relation $\lambda_s \propto \rho_s$ was respected (thermal conductivity λ_s and solid density ρ_s are linearly correlated for wood of different species [66, 67, 51]).

The specific heat capacity of the solid $c_{p,s}$ had an effect on the dynamics of the system (delay time for thermal runaway) but only mildly influenced the critical temperature within the range tested. Some influences of sample emissivity on critical temperature were observed, indicating that enhanced external heat dissipation can inhibit or delay self-ignition. Wall emissivity, sample permeability and diffusion coefficient at reference temperature did not have a notable effect on simulation predictions within the range of values investigated.

Due to the exponential nature of the Arrhenius-expression, varying activation energy may have very strong effects on modeling outcomes. The effect of E_a was therefore investigated by creating new sets of E_a and k_0, so that reaction rates $k(T)$ were equal at 470 K (see deatils in the supporting information). This is a more realistic representation of the type of errors that may be introduced during thermogravimetric analysis. Lowering E_a and adapting k_0 shifted the critical temperature for ignition quite significantly (Fig. 8). Uncertainties in kinetic parameters may be amplified in bench scale simulations [19], which appears to be the case here.

In summary, parameters for heat release rates (kinetic parameters and heat of reaction) have the largest influence on the model. As discussed elsewhere [29], kinetic parameters are difficult to determine for the temperature range of interest in self-ignition. Parameters governing thermal diffusivity $a = \lambda/(\rho\, c_p)$ have a noteworthy influence on modeling results, but values are also well-known for typical biomasses. The contribution of radiation across pores to heat transfer in porous solids, on the other hand, is difficult to quantify [19, 31], but appears to have only minor influence. Permeability of dust accumulations is also not well

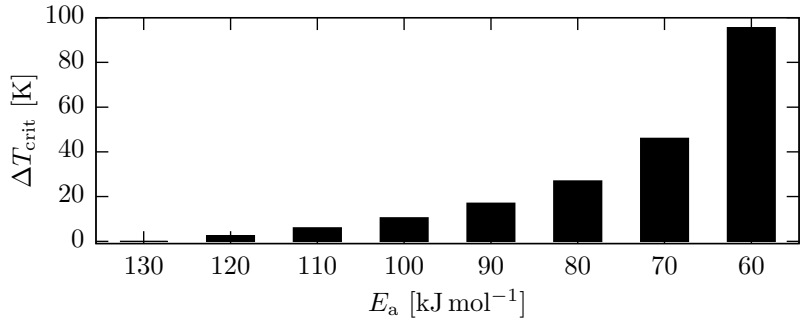

Figure 8: Sensitivity analysis: effect of varying activation energy, while keeping a constant reaction rate k at 470 K (Base case: $E_{\mathrm{a}} = 130\,\mathrm{kJ\,mol^{-1}}$ and $T_{\mathrm{crit}} = 479\,\mathrm{K}$)

researched [24, 31], but mass transfer limitations generally appear to become important only once reaction rates accelerate.

4.6. Scaling

Further isothermal simulations were carried out to investigate the effects of sample size, sample mass, bulk density, and ambient oxygen concentration. Critical temperatures for thermal runaway decreased approximately logaritmically with an increase of any of these parameters (Fig. 9). Effects of sample size were investigated by scaling all geometric lengths of the model by factors of 2, 4, 8 and 16. Gas volumetric flow rates were correspondingly scaled by 2^3, 4^3, 8^3 and 16^3 in order to keep gas velocities constant (for convective heat transfer). All other parameters were kept constant. Critical temperatures dropped by 15–20 K for every doubling of the characteristic lengths (i.e., the sample diameter). The effect appeared to level off with increasing sample size. Dust accumulations with characteristic dimensions (e.g., bed depth) of 0.05–0.1 m could plausibly approach critical conditions for temperatures above 430 K.

Sample mass effects at constant volume were calculated by varying both solid density and bulk density by factors of 0.5, 1.5, 2, 3 and 4; keeping all other parameters constant. The bed porosity remained at a constant value of $\phi = 0.8$. Calculations showed a logarithmic decrease of critical temperatures with increasing sample mass (Fig. 9b). Similarly, bed compaction was investigated

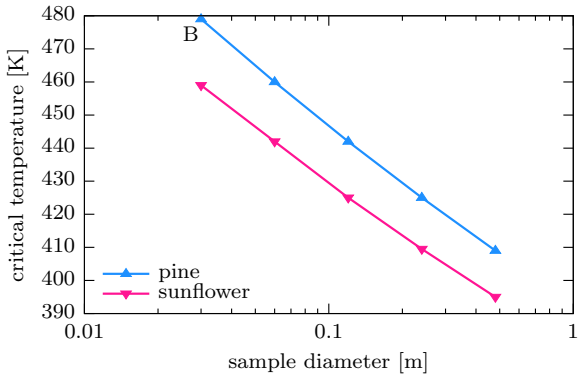

(a) Size

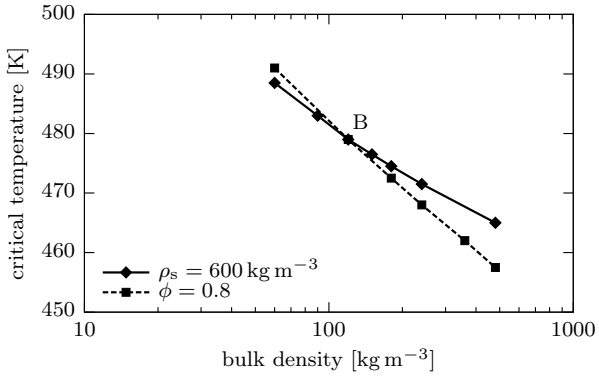

(b) Density

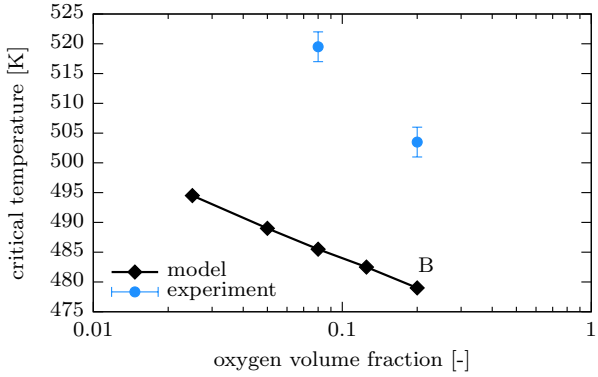

(c) Oxygen – experimental data included for comparison

Figure 9: Effect of varying sample size, solid and bulk densities, as well as ambient oxygen concentrations. Note the different ordinate scales. The data point marked B is the common base case: pine, d=0.03 m, ρ=108 kg m^{-3}, ρ_s=600 kg m^{-3}, ϕ =0.8, 20 % oxygen; T_{crit} = 479 K

by varying the bulk density a constant solid density. More compact samples (higher bulk density) had lower critical ignition temperatures. This qualitatively agrees with experimental findings: increasing sample bulk densities by a factor of 1.5 could reduce the critical temperature in the order of 5 K (see supporting information and [58]). Ambient temperatures were not varied finely enough in the experiments to draw definite conclusions from this comparison, however.

The reduced porosity allowed for higher ambient temperatures compared to the case in which a larger sample mass was achieved by a higher solid density. As ignition did not appear to be mass-transfer limited in the simulations, this effect is (numerically) due to a larger effective thermal conductivity (and thus better heat dissipation) in the dust bed for low porosities. The extrapolation should be done with care, however, as some of the modeling assumptions relating to gas transport break down for low bed porosities.

Simulations were only mildly sensitive to ambient oxygen concentrations (Fig. 9c). Increase of the critical ambient temperature when ambient oxygen is reduced is smaller than indicated by the experimental data (see also supporting information), as well as by data published for wood [68] and cork dusts [69]. Since mass transfer limitations are low, this can likely be traced to the reaction order in oxygen used in the kinetic mechanism.

5. Conclusions

A mechanistic model to describe self-heating and self-ignition under conditions typically found in power plant mills was developed. The model takes into consideration emperature gradients, gas diffusion, pyrolysis kinetics and heterogeneous oxidation kinetics. Physically correct parameters were used for all mechanisms. No fitting was involved. The model was successfully validated with a series of lab-scale fixed bed experiments that imitate mill conditions. Critical temperatures that lead to ignition could be predicted with good accuracy .

Sensitivity of the model to various parameters was analyzed. Modeling of self-ignition depends to a large degree on the heat release kinetics (Figs. 7 and

8). Parameters governing internal and external heat transfer have somewhat less influence on modeling results. Unlike kinetic parameters (especially for low termperature oxidation), these are also known with good accuracy for different biomasses. The model was least sensitive to parameters governing mass transfer, i.e. diffusion and advection in porous solids. These findings underline the necessity of determining accurate low-temperature kinetic models for the biomasses in question. Additionally, properties of biomass that promote reactions on lab-scale should also be considered as risk factors for power plant mill operation.

Sample size, bulk density and bed porosity have an influence on self-ignition (their importance given in descending order). Likely, these parameters influence heat transfer within the particle bed. Effects of particle size were not investigated here, but it is plausible that they also influence heat transfer.

Predictions indicate that critical temperatures for ignition decrease significantly with sample size. In this study, the critical teperature for ignition decreased by 15–20 K for every doubling of the sample size. These calculations suggests that large dust accumulations severly enhance the risk of self-ignition. As an estimation, dust beds with a characteristic length of 0.05–0.1 m may self-ignite from 430 K and above – in comparison, power plant mills are operated at air inlet temperatures up to 423 K (150 °C) with wood pellets. In consequence, biomass fuels should not be allowed to build up in larger heaps in power plant mills. This includes e.g. removing the fuel on shut down of the mill.

Overall, results from this work demonstrate that self-ignition experiments can be simulated based on available material properties and reaction mechanisms derived e.g. from thermogravimetric analysis. Instead of predicting self-ignition from direct extrapolation of lab-scale experiments, where transport properties and reaction kinetics are combined into single, effective reaction kinetics (e.g., according to the Frank-Kamenetskii method), this suggests models should aim for a better physical representation of ignition phenomena. Future research should especially be focused on determining more accurate reaction mechanisms for biomass at low temperatures.

Acknowledegements

The authors thank Ørsted A/S and Energinet for financial support of this work.

Symbols and abbreviations

symbol	quantity	base units
A	area	m^2
a	thermal diffusivity	$\mathrm{m}^2\,\mathrm{s}^{-1}$
C	molar concentration	$\mathrm{mol}\,\mathrm{m}^{-3}$
c_p	specific heat capacity	$\mathrm{J}\,\mathrm{kg}^{-1}\mathrm{K}^{-1}$
D	diffusion coefficient	$\mathrm{m}^2\,\mathrm{s}^{-1}$
E_a	apparent activation energy	$\mathrm{J}\,\mathrm{mol}^{-1}$
H	enthalpy	J
$\overline{H}$	mole-specific enthalpy	$\mathrm{J}\,\mathrm{mol}^{-1}$
h	specific enthalpy	$\mathrm{J}\,\mathrm{kg}^{-1}$
k	reaction rate	s^{-1}
k_0	pre-exponential factor	s^{-1}
L	length	m
M	molar mass	$\mathrm{kg}\,\mathrm{mol}^{-1}$
m	mass	kg
n	amount of substance	mol
p	pressure	Pa
Q	heat	J
R	universal gas constant	$\mathrm{J}\,\mathrm{mol}^{-1}\mathrm{K}^{-1}$
r	spatial coordinate	m
T	temperature	K
t	time	s
u	velocity	$\mathrm{m}\,\mathrm{s}^{-1}$
V	volume	m^3
w	mass fraction	$\mathrm{kg}\,\mathrm{kg}^{-1}$

X	conversion	–
y	mole fraction	$\mathrm{mol\,mol^{-1}}$
z	source term density	$\mathrm{mol\,m^{-3}\,s^{-1}}$
α	heat transfer coefficient	$\mathrm{W\,m^{-2}K^{-1}}$
γ	stoichiometric coefficient	$\mathrm{mol\,mol^{-1}}$
δ	relative error	–
ε	emissivity	–
η	dynamic viscosity	$\mathrm{Pa\,s}$
κ	permeability coefficient	$\mathrm{m^2}$
λ	thermal conductivity	$\mathrm{W\,m^{-1}K^{-1}}$
ν	apparent reaction order	–
ρ	density	$\mathrm{kg\,m^{-3}}$
σ	Stefan-Boltzmann constant	$\mathrm{W\,m^{-2}K^{-4}}$
τ	$1-\tau$: error on critical temperature	–
ϕ	porosity	–

index	meaning
0	initial
A	ash
C	carbon
c	contact
crit	critical
eff	effective
ext	external
f	final
g	gas
H	hydrogen
i	index for species
ign	ignition

j	index for species, $j \neq i$
LHV	lower heating value
O	oxygen
ox	oxidation
pyr	pyrolysis
R	reaction
r	index for reaction
ref	reference
s	solid
sim	simulated
STP	standard temperature and pressure
tot	total
W	water
w	wall

α	convection
ε	radiation
λ	conduction

superscripts

$\dot{\square}$	$\square$ per unit time (rate of $\square$)
$\square''$	$\square$ per unit area
$\square'''$	$\square$ per unit volume

[1] S. J. Gerssen-Gondelach, D. Saygin, B. Wicke, M. K. Patel, and A. P. C. Faaij. Competing uses of biomass: Assessment and comparison of the performance of bio-based heat, power, fuels and materials . *Renewable and Sustainable Energy Reviews*, 40:964–998, 2014.

[2] W. R. Livingston. The status of large scale biomass firing: The milling and combustion of biomass materials in large pulverised coal boilers. Technical report, IEA Bioenergy: Task 32: Biomass Combustion and Cofiring, 2016.

[3] P. H. Thomas and P. C. Bowes. Some aspects of the self-heating and ignition of solid cellulosic materials. *British Journal of Applied Physics*, 12:222–229, 1961.

[4] S. Krigstin and S. Wetzel. A review of mechanisms responsible for changes to stored woody biomass fuels. *Fuel*, 175:75–86, 2016.

[5] J. M. Ashman, J. M. Jones, and A. Williams. Some characteristics of the self-heating of the large scale storage of biomass. *Fuel Processing Technology*, 174:1–8, 2018.

[6] K. Savolainen. Co-firing of biomass in coal-fired utility boilers. *Applied Energy*, 74(3-4):369–381, 2003.

[7] T. Krause and Y. Al-Khasawneh. Making the switch from coal to biomass. *Cogeneration & On-Site Power Production*, 16(2):24–27, 2015.

[8] C. Birkby, J. Brown, and P. J. Street. The early detection of mill fires by monitoring for carbon monoxide. *Combustion*, 45(2):38–42, 1973.

[9] J. C. Dage and L. R. Howard. Coal pulverizer prevention for increased use of low sulfur western coal. *Proceedings of the American Power Conference*, pages 1090–1092, 1993.

[10] T. X. Ren, J. S. Edwards, and D. Clarke. Adiabatic oxidation study on the propensity of pulverised coals to spontaneous combustion. *Fuel*, 78(14):1611–1620, 1999.

[11] R. G. Zalosch. Review of Coal Pulverizer Fire and Explosion Incidents. In *Industrial Dust Explosions, ASTM STP 958*, pages 191–201. American Society for Testing and Materials, 1987.

[12] N. N. Semenoff. Zur Theorie des Verbrennungsprozesses. *Zeitschrift für Physik*, 48(7):571–582, 1928.

[13] D. A. Frank-Kamenetskii. *Diffusion and Heat Transfer in Chemical Kinetics*. Plenum Press, 2nd revised edition, 1969. English translation by J. P. Appleton.

[14] B. F. Gray, J. F. Griffiths, and S. M. Hasko. Spontaneous Ignition Hazards in Stockpiles of Cellulosic Materials: Criteria for Safe Storage. *Journal of Chemical Technology and Biotechnology A*, 34(8):453–463, 1984.

[15] J. C. Jones. On the Extrapolation of Results from Oven Heating Tests for Propensity to Self-Heating. *Combustion and Flame*, 124(1-2):334–336, 2001.

[16] U. Krause and M. Schmidt. The influence of initial conditions on the propagation of smouldering fires in dust accumulations. *Journal of Loss Prevention in the Process Industries*, 14(6):527–532, 2001.

[17] U. Krause, M. Schmidt, and C. Lohrer. A numerical model to simulate smouldering fires in bulk materials and dust deposits. *Journal of Loss Prevention in the Process Industries*, 19(2-3):218–226, 2006.

[18] M. van Blijderveen, E. A. Bramer, and G. Brem. Modelling spontaneous ignition of wood, char and RDF in a lab-scale packed bed. *Fuel*, 108:190–196, 2013.

[19] X. Huang and G. Rein. Thermochemical conversion of biomass in smouldering combustion across scales: The roles of heterogeneous kinetics, oxygen and transport phenomena. *Bioresource Technology*, 207:409–421, 2016.

[20] H. Yuan, F. Restuccia, F. Richter, and G. Rein. A computational model to simulate self-heating ignition across scales, configurations, and coal origins. *Fuel*, 236:1100–1109, 2019.

[21] A. H. Mahmoudi, F. Hoffmann, M. Markovic, B. Peters, and G. Brem. Numerical modeling of self-heating and self-ignition in a packed-bed of biomass using XDEM. *Combustion and Flame*, 163:358–369, 2016.

[22] F. Ferrero, C. Lohrer, B. M. Schmidt, M. Noll, and M. Malow. A mathematical model to predict the heating-up of large-scale wood piles. *Journal of Loss Prevention in the Process Industries*, 22(4):439–448, 2009.

[23] C. D. Everard, M. Schmidt, K. P. McDonnell, and J. Finnan. Heating processes during storage of Miscanthus chip piles and numerical simulations to predict self-ignition. *Journal of Loss Prevention in the Process Industries*, 30:188–196, 2014.

[24] R. Aganetti, A. Lamorlette, E. Guilbert, D. Morvan, and G. R. Thorpe. Advection and the self-heating of organic porous media. *International Journal of Heat and Mass Transfer*, 93:1150–1158, 2016.

[25] T. Luangwilai, H. S. Sidhu, and M. I. Nelson. One-dimensional spatial model for self-heating in compost piles: Investigating effects of moisture and air flow. *Food and Bioproducts Processing*, 108:18–26, 2018.

[26] W. Guo. *Self-Heating and Spontaneous Combustion of Wood Pellets during Storage*. PhD thesis, University of British Columbia, 2013.

[27] J. B. Howard and R. H. Essenhigh. Mechanism of solid-partical combustion with simultaneous gas-phase volatiles combustion. *Symposium (International) on Combustion*, 11(1):399–408, 1967.

[28] J. J. Saastamoinen, M. J. Aho, and V. L. Linna. Simultaneous pyrolysis and char combustion. *Fuel*, 72(5):599–609, 1993.

[29] L. Schwarzer, Z. Sárossy, P. A. Jensen, P. Glarborg, O. Karlström, J. K. Holm, and K. Dam-Johansen. Kinetic parameters for biomass under self-ignition conditions: Low-temperature oxidation and pyrolysis. *Energy & Fuels*, 33(9):8606–8619, 2019.

[30] W. J. Massman. A review of the molecular diffusivities of H2O, CO2, CH4, CO, O3, SO2, NH3, N2O, NO, and NO2 in air, O2 and N2 near STP. *Atmospheric Environment*, 32(6):1111–1127, 1998.

[31] C. W. Lautenberger. *A Generalized Pyrolysis Model for Combustible Solids*. PhD thesis, University of California, Berkeley, 2007.

[32] H. Lu, E. Ip, J. Scott, P. Foster, M. Vickers, and L. L. Baxter. Effects of particle shape and size on devolatilization of biomass particle. *Fuel*, 89(5):1156–1168, 2010.

[33] M. Lindstrom and B. Wetton. A comparison of Fick and Maxwell-Stefan diffusion formulations in PEMFC gas diffusion layers. *Heat and Mass Transfer*, 53(1):205–212, 2017.

[34] A. L. Loeb. Thermal conductivity: VIII, A theory of thermal conductivity of porous materials. *Journal of the American Ceramic Society*, 37(2):96–99, 1954.

[35] Verein Deutscher Ingenieure VDI-Gesellschaft Verfahrenstechnik und Chemieingenieurwesen (GVC), editor. *VDI-Wärmeatlas*. Springer Berlin Heidelberg, 10 edition, 2006.

[36] J. H. Ferziger and M. Perić. *Computational Methods for Fluid Dynamics*. Springer Berlin Heidelberg, 2002.

[37] R. Alén, E. Kuoppala, and P. Oesch. Formation of the main degradation compound groups from wood and its components during pyrolysis. *Journal of Analytical and Applied Pyrolysis*, 36(2):137–148, 1996.

[38] Y. Chen, S. Charpenay, A. Jensen, M. A. Wójtowicz, and M. A. Serio. Modeling of biomass pyrolysis kinetics. *Symposium (International) on Combustion*, 27(1):1327–1334, 1998.

[39] M. Olsson, O. Ramnäs, and G. Petersson. Specific volatile hydrocarbons in smoke from oxidative pyrolysis of softwood pellets. *Journal of Analytical and Applied Pyrolysis*, 71:847–854, 2004.

[40] H. Yang, R. Yan, H. Chen, D. H. Lee, and C. Zheng. Characteristics of hemicellulose, cellulose and lignin pyrolysis. *Fuel*, 86(12-13):1781–1788, 2007.

[41] M. Perzon. Emissions of organic compounds from the combustion of oats - a comparison with softwood pellets. *Biomass and Bioenergy*, 34(6):828–837, 2010.

[42] D. Shen, J. Hu, R. Xiao, H. Zhang, S. Li, and S. Gu. Online evolved gas analysis by thermogravimetric-mass spectroscopy for thermal decomposition of biomass and its components under different atmospheres: Part I. Lignin. *Bioresource Technology*, 130:449–456, 2013.

[43] D. Shen, L. Zhang, J. Xue, S. Guan, Q. Liu, and R. Xiao. Thermal degradation of xylan-based hemicellulose under oxidative atmosphere. *Carbohydrate Polymers*, 127:363–371, 2015.

[44] S. Benkorichi, T. Fateh, F. Richard, J.-L. Consalvi, and A. Nadjai. Investigation of thermal degradation of pine needles using multi-step reaction mechanisms. *Fire Safety Journal*, 91:811–819, 2017.

[45] Energy Research Centre of the Netherlands. Phyllis2, database for biomass and waste. https://www.ecn.nl/phyllis2.

[46] P. J. Linstrom and W. G. Mallard, editors. *NIST Chemistry Webook, NIST Standard Reference Database Number 69*. National Institute of Standards and Technology, 2018.

[47] J. Rath, M. G. Wolfinger, G. Steiner, G. Krammer, F. Barontini, and V. Cozzani. Heat of wood pyrolysis. *Fuel*, 82(1):81–91, 2003.

[48] C. Di Blasi. Modeling chemical and physical processes of wood and biomass pyrolysis. *Progress in Energy and Combustion Science*, 34(1):47–90, 2008.

[49] B. M. Suleiman, J. Larfeldt, B. Leckner, and M. Gustavsson. Thermal conductivity and diffusivity of wood. *Wood Science and Technology*, 33(6):465–473, dec 1999.

[50] J. Sjöström and P. Blomqvist. Direct measurements of thermal properties of wood pellets: Elevated temperatures, fine fractions and moisture content. *Fuel*, 134:460–466, 2014.

[51] P. E. Mason, L. I. Darvell, J. M. Jones, and A. Williams. Comparative study of the thermal conductivity of solid biomass fuels. *Energy & Fuels*, 30(3):2158–2163, 2016.

[52] K. W. Ragland, D. J. Aerts, and A. J. Baker. Properties of wood for combustion analysis. *Bioresource Technology*, 37(2):161–168, 1991.

[53] M. Gupta, J. Yang, and C. Roy. Specific heat and thermal conductivity of softwood bark and softwood char particles. *Fuel*, 82(8):919–927, 2003.

[54] W. Guo, C. J. Lim, X. Bi, S. Sokhansanj, and S. Melin. Determination of effective thermal conductivity and specific heat capacity of wood pellets. *Fuel*, 103:347–355, 2013.

[55] C. Dupont, R. Chiriac, G. Gauthier, and F. Toche. Heat capacity measurements of various biomass types and pyrolysis residues. *Fuel*, 115:644–651, 2014.

[56] H. D. Baehr and K. Stephan. *Wärme- und Stoffübertragung.* Springer Berlin Heidelberg, 2010.

[57] H. R. Wesson, J. R. Welker, and C. M. Sliepcevich. The piloted ignition of wood by thermal radiation. *Combustion and Flame*, 16(3):303–310, 1971.

[58] L. Schwarzer. *Biomass Particle Ignition in Mill Equipment*. PhD thesis, DTU Chemical Engineering, 2019.

[59] M. A. Rahman and P. K. Hopke. Mechanistic pathway of carbon monoxide off-gassing from wood pellets. *Energy and Fuels*, 30:5809–5815, 2016.

[60] E. Alakoski, M. Jämsén, D. Agar, E. Tampio, and M. Wihersaari. From wood pellets to wood chips, risks of degradation and emissions from the storage of woody biomass – a short review. *Renewable and Sustainable Energy Reviews*, 54:376–383, 2016.

[61] S. Moqbel, D. Reinhart, and R.-H. Chen. Factors influencing spontaneous combustion of solid waste. *Waste Management*, 30(8-9):1600–1607, 2010.

[62] A. Ronda, M. Della Zassa, A. Biasin, M. A. Martin-Lara, and P. Canu. Experimental investigation on the smouldering of pine bark. *Fuel*, 193:81–94, 2017.

[63] C. Lohrer, M. Schmidt, and U. Krause. A study on the influence of liquid water and water vapour on the self-ignition of lignite coal-experiments and numerical simulations. *Journal of Loss Prevention in the Process Industries*, 18(3):167–177, 2005.

[64] R. Jackson. *Transport in porous catalysts*. Number 4 in Chemical engineering monographs. Elsevier, 1977.

[65] I. I. Kantorovich and E. Bar-Ziv. Heat transfer within highly porous chars: a review. *Fuel*, 78(3):279–299, 1999.

[66] L. W. Austin and C. W. Eastman. On the relation between heat conductivity and density in some of the common woods. *Wisconsin Academy of Sciences, Arts and Letters. Transactions*, pages 539–542, 1900.

[67] H. Thunman and B. Leckner. Thermal conductivity of wood—models for different stages of combustion. *Biomass and Bioenergy*, 23(1):47–54, 2002.

[68] P. C. Bowes and P. H. Thomas. Ignition and Extinction Phenomena Accompanying Oxygen-dependent Self-heating of Porous Bodies. *Combustion and Flame*, 10(3):221–230, 1966.

[69] M. Schmidt, C. Lohrer, and U. Krause. Self-ignition of dust at reduced volume fractions of ambient oxygen. *Journal of Loss Prevention in the Process Industries*, 16(2):141–147, 2003.